Polymer Chemistry

ROYAL SOCIETY OF CHEMISTRY

PAPER

View Article Online
View Journal | View Issue

Check for updates

Cite this: *Polym. Chem.*, 2022, **13**, 3892

Donor modification of thermally activated delayed fluorescence photosensitizers for organocatalyzed atom transfer radical polymerization†

Alexander M. Polgar, Shine H. Huang and Zachary M. Hudson *

Received 12th April 2022,
Accepted 4th June 2022

DOI: 10.1039/d2py00470d

rsc.li/polymers

Thermally activated delayed fluorescence (TADF) photosensitizers based on 9,10-dihydro-9,9-dimethyl-acridine/2,4,6-triphenylpyrimidine conjugates with strong visible absorption, large excited state reduction potentials, and long-lived triplet excited states were successfully employed in the organocatalyzed atom transfer radical polymerization (O-ATRP) of methacrylic monomers. A donor-modification strategy dramatically improved the stability of the photocatalyst radical cations, while retaining their high oxidizing strengths, a key requirement for controlled O-ATRP. Time-resolved photoluminescence studies of the catalysts support initiation by electron transfer from both singlet and triplet states, with functionalized donors producing higher driving forces for photoinduced electron transfer. A donor-modified TADF photocatalyst was found for the synthesis of methacrylic polymers with *Đ* below 1.3 at catalyst loadings down to 50 ppm. This catalyst was also successfully applied in block copolymer synthesis, while the unfunctionalized analogue yields entirely uncontrolled polymerization.

1. Introduction

Controlled radical polymerizations such as nitroxide-mediated polymerization (NMP),[1] radical addition–fragmentation chain transfer (RAFT),[2] and atom-transfer radical polymerization (ATRP)[3] have empowered chemists to synthesize polymers of well-defined size, composition, and topology without the need for specialized equipment.[4] In ATRP, polymerization is mediated by a metal complex (commonly Cu) which reversibly deactivates propagating radical chains through an inner-sphere single electron transfer.[5] Initially, very high loadings (>1000 ppm) of Cu were required to achieve sufficient rates of polymerization, raising issues with the applicability of the technique in biomedicine, health/beauty products, and electronics.[6] Lower Cu loadings (10–50 ppm) have since been realized by the addition of supplemental initiators or reducing agents to the polymerization to continuously regenerate the Cu^I activator.[6–9]

Yagci and others have demonstrated the suitability of photoredox catalysis to mediate Cu ATRP with reduced catalyst loadings.[10–13] The excited states of photosensitizers are powerful electron donors that can regenerate Cu^I through an oxidative quenching process, with a sacrificial electron donor to complete the catalytic cycle. In 2012, Hawker demonstrated photomediated ATRP with an iridium photocatalyst (PC) that reduces alkyl halide ATRP initiators from its excited state (PC*), generating a highly oxidizing photocatalyst radical cation ($PC^{•+}$) that controls polymerization by deactivating the propagating radical.[14] This obviated the need for both a Cu^I activator and a sacrificial electron donor. Purely organic O-ATRP followed from the same group, using 10-phenylphenothiazine as a potent excited state reductant.[15] Further development of O-ATRP has seen various phen(ox)azine derivatives and heteroatom-doped aromatic hydrocarbons find use as visible-light activated photocatalysts, which may be applied at reduced loadings, over a wide monomer scope, and under irradiation from sunlight.[16–21] As a result of these innovations, photoinduced electron transfer (PET) has become a key feature of metal-free reversible deactivation radical polymerizations.[22–26]

In 2017, Huang *et al.* demonstrated O-ATRP using thermally activated delayed fluorescence (TADF) emitters as photocatalysts.[27] TADF is widely deployed in fields ranging from organic electronics,[28] photocatalysis,[29] biological imaging,[30] and chemical sensing[31,32] due to a unique ability to interconvert singlet and triplet excited states. TADF emitters are commonly designed around a twisted donor–π–acceptor (D–π–A) motif to minimize overlap between the electron density of the HOMO and LUMO. This reduces the electronic exchange energy between electrons in the excited biradical state. Consequently, there is a small energetic gap between the first excited singlet

---

Department of Chemistry, The University of British Columbia, 2036 Main Mall, Vancouver, British Columbia, V6T 1Z1, Canada. E-mail: zhudson@chem.ubc.ca; Fax: +1-604-822-2847; Tel: +1-604-822-3266

† Electronic supplementary information (ESI) available. See DOI: **https://doi.org/10.1039/d2py00470d**

(S_1) and triplet (T_1) states that may be overcome by thermal energy in a process termed reverse intersystem crossing (RISC). The result is a cycling between S_1 and T_1 that prolongs the excited state lifetime and facilitates singlet and triplet energy/electron transfer.[33]

The benefits of TADF emitters for O-ATRP were clearly demonstrated by Singh *et al.* in 2018.[34] Through computational screening, and detailed structure–activity relationships, the authors identified the TADF emitter 2,4,5,6-tetrakis(diphenylamino)-1,3-benzenedicarbonitrile (4DPIPN) as an optimal photocatalyst for the polymerization of methyl methacrylate (MMA) at sub-ppm catalyst loadings. Due to the prolonged excited state lifetime of TADF emitters, the effective concentration of the excited state activator species in solution is higher than for a comparable concentration of a fluorescent photosensitizer.[14] At the low catalyst loadings afforded by TADF catalysis, the polymer formed might be used without catalyst removal – greatly simplifying the procedure compared to conventional Cu-based ATRP.

The donor–acceptor nature of TADF has advantages for achieving controlled O-ATRP with an expanded monomer scope. As shown in Fig. 1, the charge transfer (CT) excited state of a TADF emitter with a D–π–A design can be approximated as a biradical with an oxidized donor ($D^{\bullet+}$) and reduced acceptor ($A^{\bullet-}$). In the activation step of O-ATRP, the excited state undergoes oxidative quenching with an alkyl halide initiator. The driving force for this step is proportional to the reduction potential of the ground-state acceptor. Singh *et al.* made use of this fact, using the weak acceptor diphenylsulfone, with a large negative ground-state reduction potential ($E°(A/A^{\bullet-})$ = −2.3 V *vs.* SCE) for the controlled O-ATRP of styrene ($E°(RBr/R^{\bullet} + Br^-) \sim -1.5$ V; R = α-alkyl benzyl).[34] Moreover, if electron transfer from the excited triplet state is dominant in an O-ATRP, the small ΔE_{ST} of TADF PCs allows less excitation energy to be lost *via* ISC – a unique feature of TADF photosensitizers.

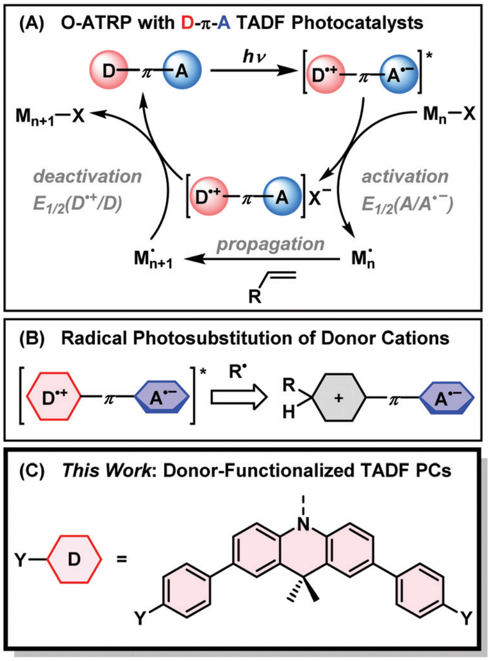

Fig. 1 (A) Mechanism of organocatalyzed atom-transfer radical polymerization of olefinic monomers using D–π–A type photocatalysts. (B) Deactivation of charge transfer excited states by radical substitution at the donor. (C) Functionalized 9,10-dihydro-9,9-dimethylacridine donors used in this work.

Matyjaszewski argued that deactivation of the propagating radical occurs through a termolecular encounter involving an associative electron transfer (AET) with the photocatalyst radical cation.[35] Weaker donors, with higher oxidation potentials ($E°(D^{\bullet+}/D)$), therefore provide a larger driving force for this step, and should yield greater control over polymer molecular weight and dispersity. TADF photocatalysts are unique in the ability to independently tune the driving force for activation and deactivation through choice of donor and acceptor moieties. The ideal TADF photocatalyst needs to balance the opposing demands of fast activation and deactivation (requiring weak donors and acceptors) with intense visible light absorption from a charge transfer excited state – which conversely relies on using stronger donors and acceptors.

Using electron donors and acceptors in photoredox catalysis comes with the drawback of unwanted excited state side reactivity.[36] Exposed positions on the aromatic rings of catalysts with electron donor moieties can abstract radicals from the polymerization (Fig. 1B).[27,37–39] This lowers the initiator efficiency of the reaction and can also deactivate the catalyst towards further photocatalytic cycling by changing its light-absorbing and electrochemical properties. König has shown that the acceptor is also vulnerable to radical photosubstitution chemistry in cyanobenzene-based catalysts such as 4DPIPN.[40,41] Weak C–S and C–P bonds are also subject to cleavage in sulfone- or phosphine-oxide-based acceptors.[42] Degradation of the acceptor might be mitigated by instead using electron-deficient nitrogen-based heterocycles, as any degradation of the acceptor would occur at a lower rate due to the disruption of aromaticity.

Here, we propose the use of donor-modified TADF emitters as photocatalysts for O-ATRP. Our design is based around 2,4,6-triphenylpyrimidine acceptors, having a high ground state reduction potential ($E°(A/A^{\bullet-})$ = −1.7 V *vs.* SCE), and 9,10-dihyro-9,9-dimethylacridine donors with strongly oxidizing radical cations ($E°(D^{\bullet+}/D) \geq 0.7$ V) in the donor–acceptor conjugate. To limit excited state side-reactivity and improve the visible light absorption of the CT excited state, methylbenzene and methoxybenzene groups are appended to the *para*-positions of 9,10-dihyro-9,9-dimethylacridine (Fig. 1C). The donor-modified photocatalysts significantly outperform the catalyst without *para*-substitution, allowing for the polymerization of MMA and benzyl methacrylate (BnMA) with dispersities down to 1.27 at 50 ppm catalyst loading. Time-resolved fluorescence studies reveal rapid and near-quantitative electron transfer from the triplet state of the photocatalyst, with increased rates for the donor-modified catalysts that have higher driving forces for photoinduced electron transfer. The chain-end fidelity of the polymerization was corroborated by the synthesis of a block copolymer with high chain re-initiation efficiency. Overall, this work demonstrates the promise of molecular engineering for TADF emitters in photoredox-mediated controlled radical polymerizations.

2. Experimental

2.1 Instrumentation

2.1.1 Nuclear magnetic resonance and mass spectrometry. ^{1}H and ^{13}C{^{1}H} nuclear magnetic resonance (NMR) spectra were measured on a Bruker AV III HD 400 MHz spectrometer. Chemical shifts are initially referenced to Me_4Si external standard and then internally to residual (proteo-)solvent signals. DOSY experiments were performed at 25 °C in $CDCl_3$ using the standard pulse program ledbpgp2s from Bruker. A bipolar gradient pulse pair was used with a total duration of 2.5 ms and a diffusion time of 100 ms. The number of gradient steps was 128. Data were processed in MestReNova Version 14.0.0 using a Bayesian DOSY transform. High-resolution mass spectra were measured by electrospray ionization (APCI, Waters/Micromass LCT).

2.1.2 Optical spectroscopy. Absorbance measurements were made on a Cary 60 spectrometer, and fluorescence measurements were made on an Edinburgh Instruments FS5 spectrofluorometer in standard 1 cm quartz cells. Absolute photoluminescence quantum yields were determined on nitrogen-sparged samples in toluene by using an Edinburgh Instruments SC-30 Integrating Sphere Module. Time-correlated single photon counting (TCSPC) measurements were made on the same FS5 spectrofluorometer with a 313 nm or 380 nm picosecond pulsed LED (Edinburgh Instruments) excitation source. Phosphorescence measurements were performed in glassy 2-methyltetrahydrofuran at 77 K using an Edinburgh Instruments FLS-1000 with the sample excited by a xenon flashlamp at 100 Hz. Virtual gating was used to remove fluorescence signals.

Stern–Volmer quenching experiments were carried out in reagent grade (≥99%) *N*,*N*-dimethylacetamide (DMAc), dried over 3 Å molecular sieves and subjected to three freeze–pump–thaw cycles prior to storage in a nitrogen-filled glovebox. Prior to use, DMAc was filtered through a short column of activated neutral alumina. Appropriate amounts of photocatalyst and initiator stock solutions were combined to give 100 μM of the photocatalyst and 10–200 mM of the initiator. The solution was transferred to a quartz cuvette and sealed with a custom-made screw-cap with an O-ring seal to prevent oxygen quenching. Prompt and delayed fluorescence lifetimes were modelled by exponential reconvolution fitting with the instrument response function by optimizing the χ^2 value of the fit.

2.1.3 Cyclic voltammetry. Cyclic voltammograms were collected by using a BASi Epsilon Eclipse potentiostat. A three-electrode setup was employed where the working electrode was a 3 mm diameter glassy carbon electrode, the counter electrode was a 0.5 mm platinum wire, and the reference electrode used was Ag/AgCl in aqueous KCl. A 4 mM solution of each of the photocatalysts was prepared in an electrolyte solution of 0.2 M tetrabutylammonium hexafluorophosphate in chloroform; the solution was degassed with N_2 immediately before collecting the data. The cyclic voltammetry experiments were performed at scan rates between 10 and 200 mV s^{-1}, and the potentials were internally referenced *versus* the half-wave potential of the ferrocene/ferrocenium ($Fc^{0/+}$) redox couple. These values were then converted to the standard calomel electrode (SCE), using a value of 0.4 V for $Fc^{0/+}$ *versus* the SCE.[43]

2.1.4 Size exclusion chromatography. Size exclusion chromatography was conducted in chromatography-grade THF at concentrations of 0.5–2.5 mg mL^{-1} using a Malvern OMNISEC GPC instrument equipped with a Viscotek TGuard guard column (CLM3008) and Viscotek T3000 (CLM3003) and T6000 (CLM3006) GPC columns packed with porous poly (styrene-*co*-divinylbenzene) particles regulated at a temperature of 35 °C. The signal response was measured by using differential refractive index, right-angle and low-angle light scattering detectors. Molecular weights were determined from the scattering data and the d*n*/d*c* of the polymers in tetrahydrofuran (p(BnMA) 0.164; PMMA 0.085).

2.2 Chemical synthesis

Details on the synthesis and NMR/HR-MS characterization of the photocatalysts used in this study can be found in the ESI.†

2.3 Photopolymerization procedure

Photopolymerizations were conducted in a nitrogen-filled glovebox. The light source was a 435 ± 10 nm LED strip (DIY LED U-HOME SMD2835-60led) arranged along the inside of a 6-inch diameter crystallization dish. The total light output is estimated at 1 W (200 LEDs × 5 mW per LED). The setup was continuously cooled using a fan and the glovebox atmosphere is recirculated through a cold-water heat exchanger to maintain an average temperature between 28 and 30 °C over the course of the polymerization. The polymerizations were conducted in Teflon-septum-capped 1-dram vials, which were positioned 2 inches away from the edge of the crystallization dish. The dish was set on a magnetic stir plate set to 400 rpm. A photograph of the setup and the spectrum of the LED source are shown in Fig. S1 of the ESI.†

The solvent used for photopolymerizations was DMAc (99% ACS Reagent Grade), which was degassed by three freeze–pump–thaw cycles and stored over 3 Å molecular sieves inside the glovebox. Directly before use in polymerizations, the solvent was passed through a short column of activated neutral alumina. All monomers were degassed by three freeze–pump–thaw cycles prior to use and passed through activated neutral alumina to remove inhibitor.

In a typical procedure, 100 μL of the monomer were added to a 1-dram vial containing a magnetic stir bar. Stock solutions of the initiator and photocatalyst were prepared at 50 and 2.5 or 0.5 mg mL^{-1} in DMAc, respectively. Appropriate amounts of the stock solutions were added to give theoretical DP of 200 (MMA) or 100 (BnMA) and catalyst loadings of 500

(2.5 mg mL^{-1} stock), 50, 25, and 10 ppm (0.5 mg mL^{-1} stock; ppm relative to monomer). DMAc was then added to each polymerization so that the total volume of solvent was 250 μL. The LED was then turned on and reaction kinetics were monitored by periodically removing 15 μL aliquots from the reaction, diluting in $CDCl_3$ and analyzing by NMR the relative intensity of the monomer *vs.* polymer peaks. Polymers were isolated by pipetting the reaction mixture into ethanol and collecting the precipitate by vacuum filtration.

2.4 Density functional theory

Density functional theory calculations were carried out in Gaussian 16 rev B.01. All photocatalysts were optimized at the B3LYP/6-31G(d) level of theory in their ground singlet (S_0), excited triplet (T_1) and radical cation doublet (D^+) electronic states.[44,45] Frequency analysis verified that all structures were at local minima. Ground and excited state oxidation potentials were computed from the Gibbs free energies. $\Delta G(PC^{\bullet +}/PC) = G(D^{\bullet +}) - G(S_0)$; $\Delta G^*(PC^{\bullet +}/{}^3PC^*) = G(D^{\bullet +}) - G(T_1)$. Free energies were converted into electrode potentials by taking a value of −100.5 kcal mol^{-1} for the standard hydrogen electrode.[46] Finally, a value of 0.24 V *vs.* SHE was assumed for the SCE.[43] Gas-phase B3LYP/6-31G(d) provided good agreement between theoretical and measured ground and excited state electrode potentials, within 0.3 eV. Additional diffuse or polarization functions or an implicit solvent model (DMAc) worsened the agreement between theory and experiment.

Time-dependent DFT was performed at the ωB97XD/6-311++G(d,p) level of theory using a conductor-like polarizable continuum (CPCM) solvent model, with toluene as the solvent.[47] The range-separation parameter *ω* was chosen through comparison of the theoretical charge transfer transition energy with experiment. The vertical singlet–triplet gap was determined using the Tamm–Dancoff approximation (TDA) at the optimized S_0 geometry as the difference between the energy of the lowest excited singlet and lowest excited triplet state.[48] TDA was employed to avoid underestimation of the triplet energy.[49,50]

3. Results and discussion

3.1 Catalyst design

Three D–π–A–π–D triads of 9,10-dihydro-9,9-dimethylacridine (DMA) and 2,4,6-triphenylpyrimdine (Pym) were synthesized (Section S1 of the ESI†), with the donor either bearing hydrogen atoms (**PymDMA**), methylphenyl groups (**PymDMDTA**), or methoxyphenyl (**PymDMDMA**) groups *para-* to the nitrogen atom (Fig. 2). Evaluation of their catalytic properties began by simulating their energetics in the singlet ground (S_0), excited triplet (T_1) and cationic doublet (D^+) states at the B3LYP/6-31G (d) level of theory (Fig. 2B). The Gibbs free energies of the T_1

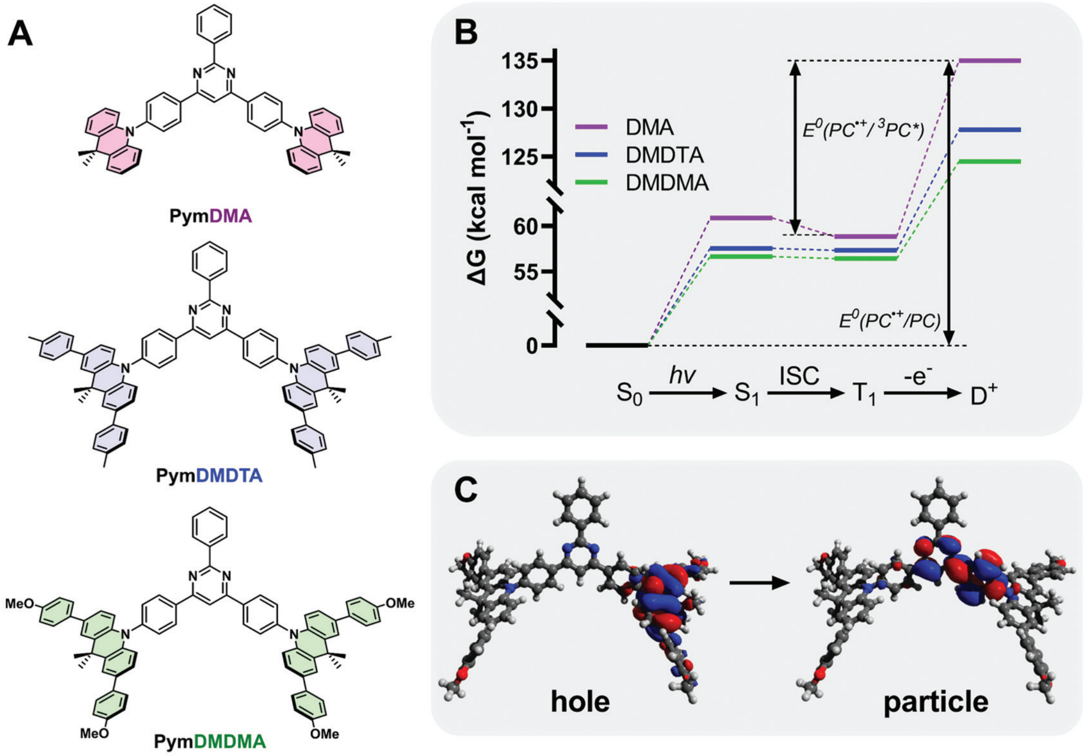

Fig. 2 (A) Structure of the photocatalysts used in this study. (B) Calculated changes in free energy during the photocatalytic cycle at B3LYP/6-31G (d) level of theory. (C) Visualization of the particle–hole pair for the S_1 transition of **PymDMDMA** at ωB97XD/6-311++g(d,p) level of theory with toluene CPCM.

state are highest for **PymDMA** at 58.9 kcal mol^{-1} above the ground state and lowest for **PymDMDMA**, bearing electron-donating methoxy groups, at 56.4 kcal mol^{-1}. The energies of the doublets vary more widely, with **PymDMA** having a high-energy radical cation at 135.0 kcal mol^{-1}, compared to 124.5 for **PymDMDMA**. The relative instability of the unmodified DMA radical cation can be expected to result in a lower driving force for photoinduced electron transfer.

The computed triplet excited state reduction potentials $E°(PC^{•+}/^3PC^*)$ are compiled in Table 1. **PymDMA**, as expected, has the lowest driving force for PET and **PymDMDMA** the highest. Nevertheless, all PCs are predicted to be sufficiently strong excited-state reductants to activate typical α-bromo ester ATRP initiators. Conversely, the unstable radical cation of **PymDMA** should provide the most rapid deactivation due to its high electron affinity $E°(PC^{•+}/PC)$ = 1.25 V *vs.* SCE. Based on these results alone, **PymDMA** should provide the best control over O-ATRP, by limiting the concentration of propagating radicals through slow activation, and reducing their persistence time with fast deactivation.

TDA-DFT was employed to calculate the singlet–triplet energy gap (ΔE_{ST}) and from this obtain an estimate of the energy of S_1. To minimize the delocalization error in density functional theory,[51] a range-separated hybrid functional ωB97XD, with variable amount of Hartree–Fock exchange, was used in conjunction with a diffuse basis set 6-311++G(d,p) to adequately describe charge transfer. Through optimization of the range-separation parameter, ω, the singlet–triplet gap of TADF emitters can be accurately predicted.[52] **PymDMDTA** and **PymDMDMA** have ΔE_{ST} below 10 meV, consistent with previous results showing that π-extended donors are effective for minimizing HOMO–LUMO overlap and ΔE_{ST}.[53,54] **PymDMA** has a higher ΔE_{ST} of 86 meV, which results in a higher-energy singlet state and corresponding greater driving force for singlet electron transfer.

The charge-transfer nature of the singlet excited states was confirmed through natural transition orbital (NTO) analysis (Fig. 2C). The first optically bright ($f > 0$) transition locates the electron density "hole" on the DMA donor, with small contributions from the *para*-aryl substituents. The "particle" is localized mainly on the pyrimidine acceptor and the phenyl bridge between the donor and acceptor. Some degree of hole–particle overlap is desirable for increased absorptivity of the lowest-energy charge transfer state, and this is observed in all cases on the phenyl bridge. Owing to their low ΔE_{ST} and strong excited-state charge-transfer nature, these materials are expected to be effective mediators of reverse intersystem crossing for efficient TADF.

3.2 Optical and electrochemical characterization

UV-vis absorption spectroscopy of all catalysts in toluene (Fig. 3A) shows moderately strong charge-transfer bands ($\varepsilon_{max} \sim 4–6 \times 10^3$ M^{-1} cm^{-1}) between 350 and 450 nm. As predicted by DFT, **PymDMA** has the highest-energy excitation to S_1, peaking at 378 nm with the band extending to 440 nm. The donor-modified derivatives have bathochromically shifted absorptions, with the charge-transfer band extending to 460 nm. All three have sufficient absorption in the visible range, due to the moderate donor and acceptor strengths of DMA and Pym, respectively.

Bright photoluminescence is observed in aerated toluene (Fig. 3B) which increases 4–5 fold when the solutions are sparged with N_2 (Fig. S2†). The relatively broad and featureless bands are typical of emission from charge-transfer excited states. The emission peak is bathochromically shifted as electron donating groups are appended to the donor. This indicates that donor-modification can enhance donor strengths, as has been shown elsewhere using carbazole as the "parent" donor.[53,54] Time-resolved emission spectra taken at 77 K in 2-methyltetrahydrofuran (2-MeTHF) reveal no difference in the onsets of prompt fluorescence and phosphorescence after a 10 ms delay (Fig. 3C and D). This indicates a near-degeneracy of the S_1 and T_1 states, consistent with DFT, which is necessary to facilitate RISC.

Time-correlated single-photon counting (TCSPC) further supports the TADF mechanism of emission for donor-modified derivatives. Microsecond-timescale emission is observed in N_2-sparged toluene, which disappears upon aerating the solution (Fig. 3E and F; see also Fig. S3†). Temperature-dependent photoluminescence decays of **PymDMDTA** and **PymDMDMA** show the expected increase in delayed emission as the temperature increases from 77 K to 298 K (Fig. S4†). **PymDMA** is a known TADF emitter with a ΔE_{ST} of 0.19 eV.[55,56] The delayed fluorescence of **PymDMA** was remeasured in toluene and a lifetime of 29.6 μs was obtained (Fig. S5†), in reasonable agreement with a previous result of 20.7 μs in DPEPO film.[55,56]

The stability of the radical cation produced in O-ATRP was studied by cyclic voltammetry. Matyjaszewski and others have shown that radical cation stability is a key determining factor in controlling O-ATRP, as the persistence of $PC^{•+}$ in solution is directly correlated to the rate of deactivation.[35] **PymDMA** undergoes irreversible oxidation, producing a secondary species that is reduced at lower cathodic potentials (Fig. 3G). In contrast, **PymDMDTA** and **PymDMDMA** both show reversible oxidations at lower potentials than **PymDMA**, agreeing

Table 1 Computed electronic properties of the PCs

	$E°(PC^{•+}/PC)$ (V *vs.* SCE)	$E°(PC^{•+}/^1PC^*)$ (V *vs.* SCE)	$E°(PC^{•+}/^3PC^*)$ (V *vs.* SCE)	ω ($Bohr^{-1}$)	ΔE_{ST} (meV)
PymDMA	1.25	−1.39	−1.30	0.1246	86
PymDMDTA	0.94	−1.55	−1.54	0.1005	9
PymDMDMA	0.80	−1.66	−1.65	0.1121	9

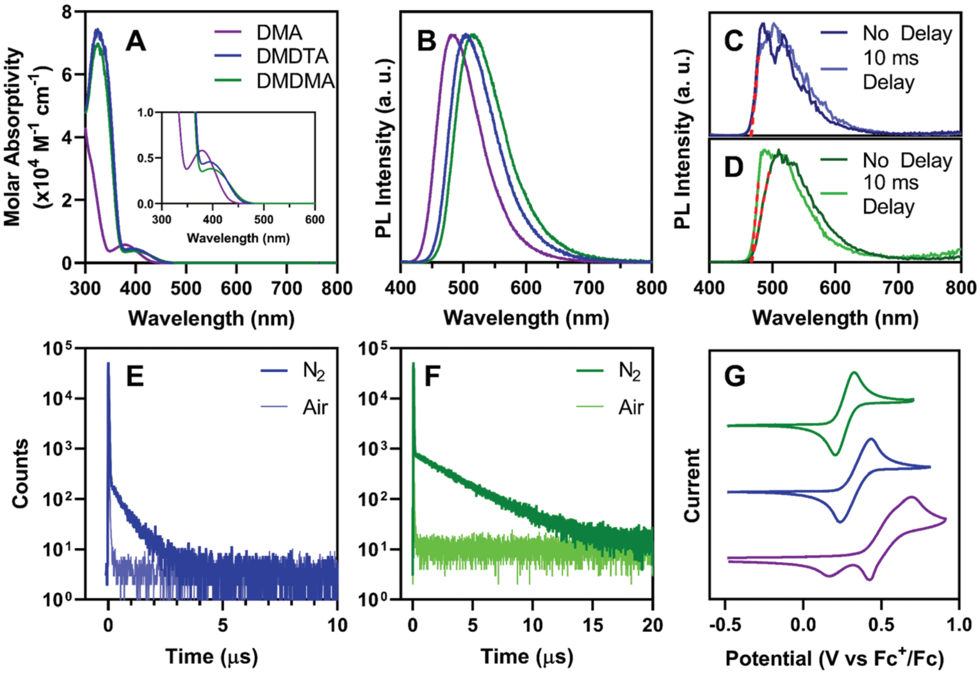

Fig. 3 (A) UV-vis spectroscopy of all photocatalysts at 50 μg mL^{-1} in toluene. (B) Fluorescence spectroscopy of photocatalysts at 2 μg mL^{-1} in toluene, excited at 380 nm. Comparison of prompt fluorescence and phosphorescence of (C) **PymDMDTA** and (D) **PymDMDMA** in 2-MeTHF (2 μg mL^{-1}) at 77 K, excited at 365 nm. Transient photoluminescence decays of (E) **PymDMDTA** and (F) **PymDMDMA** in degassed or aerated toluene (2 μg mL^{-1}), excited at 313 nm. (G) Cyclic voltammetry of all photocatalysts at 4 mM in chloroform with 200 mM (^{n}Bu$_4$N)PF$_6$ supporting electrolyte. The scan rate was 20 mV s^{-1} and the first scan is presented.

with the DFT-predicted values within 0.3 eV. Excellent reversibility is maintained over five successive cycles and is further attested to by the linearity in plots of peak anodic current *versus* the square root of the scan rate (Fig. S6 and S7†). The results are congruent with those of Miyake and co-workers,[18] suggesting that addition to the radical cation of DMA occurs through the *para*-position, and may be prevented through core modifications.

The excited state reduction potentials were estimated using $E°(\mathrm{PC}^{\bullet+}/{}^1\mathrm{PC}^*) = E°(\mathrm{PC}^{\bullet+}/\mathrm{PC}) - E_{0,0}$, where $E_{0,0}$ is the relaxed S_1 energy, estimated from the onset of fluorescence in 2-methyltetrahydrofuran at 77 K. In all cases, reduction occurs between −1.6 and −1.8 V, in good agreement with DFT. The donor-modified derivatives are stronger excited-state reductants by ~0.1 V than **PymDMA**, which should lend them faster rates of activation. The ground-state reduction potential of 2,4,6-triphenylpyrimidine was measured at −1.7 V *vs.* SCE in *N*,*N*-dimethylformamide (Fig. S8†), validating the model of PET from the $\mathrm{Pym}^{\bullet-}$ radical anion formed by photoinduced intramolecular charge transfer.

The measured photophysical and electrochemical parameters in degassed toluene and chloroform, respectively, are summarized in Table 2. Owing to the relatively low emission efficiency of **PymDMDMA**, the yield of intersystem crossing and rate of reverse intersystem crossing were calculated using an exact analysis provided by Adachi and co-workers, which does not rely on *a priori* assumptions about emission efficiency, other than the assumption of no radiative T_1 decay.[57] From this analysis, **PymDMDMA** is likely the most active catalyst for O-ATRP, with a high intersystem crossing yield, moderate rate of reverse intersystem crossing, strong driving force for photoelectron transfer and good visible light

Table 2 Measured electrochemical properties of the PCs in degassed chloroform (4 mM) and photophysical properties in degassed toluene (2 μg mL^{-1}). k_{RISC} is calculated under the assumption that $T_1 \rightarrow S_0$ transitions are negligible

	$E°(\mathrm{PC}^{\bullet+}/\mathrm{PC})$ (V *vs.* SCE)	$E°(\mathrm{PC}^{\bullet+}/{}^1\mathrm{PC}^*)$ (V *vs.* SCE)	λ_{abs}[a] (nm); ε ($\mathrm{M}^{-1}\ \mathrm{cm}^{-1}$)	λ_{em}[b] (nm); φ_{PL}	τ_{p}[c] (ns)	τ_{d}[d] (μs)	φ_{ISC}[e]	k_{RISC}[f] ($\times10^6\ \mathrm{s}^{-1}$)
PymDMA	0.96	−1.67	378; 5800	483; 0.85	16	30	0.39	0.05
PymDMDTA	0.74	−1.76	395; 4500	503; 0.73	15	0.59	0.22	1.14
PymDMDMA	0.67	−1.79	398; 3900	517; 0.47	18	3.2	0.65	0.56

[a] Wavelength of maximum absorption and molar extinction coefficient at λ_{abs}. [b] Wavelength of maximum emission and photoluminescence quantum yield. [c] Prompt fluorescence lifetime. [d] Delayed fluorescence lifetime. [e] Intersystem crossing yield. [f] Rate of reverse intersystem crossing.

absorption. **PymDMA** should offer the best control due to its slower activation and larger driving force for deactivation, however its unstable radical cation will likely prevent the establishment of an ATRP equilibrium.

3.3 Kinetics of electron transfer

To mimic typical O-ATRP conditions, the photophysical properties of the PCs were examined in deoxygenated DMAc. The intramolecular charge transfer nature of the PC excited states results in bathochromic shifting of the emission maxima to ~600 nm, compared to toluene. The photoluminescence quantum yields are reduced to between 9% for **PymDMA** and 0.9% for **PymDMDMA**, indicative of enhanced non-radiative relaxation of the excited states. This is accompanied by a reduction in the prompt and delayed fluorescence lifetimes of the PCs in DMAc, relative to toluene (Table 3). Stern–Volmer quenching experiments were then carried out for each of the PCs, using diethyl 2-bromo-2-methylmalonate (DBMM) and degassed DMAc as typical O-ATRP initiator and solvent, respectively (Fig. 4). Adding the initiator results in a progressive decrease in the delayed fluorescence lifetime, which can be fit to a linear increase in τ_0/τ with increasing DBMM concentration (where τ_0 is the lifetime in absence of the initiator and τ is the lifetime at a given [DBMM]).

On the nanosecond timescale, a slight reduction in the prompt fluorescence lifetime is also observed (Fig. S9†). The effect is most pronounced for **PymDMA**, for which the lifetime decreases from 13.0 ns in the absence of initiator to 11.4 at 200 mM DBMM. This suggests, as has been argued elsewhere, that electron transfer from both singlet and triplet excited

Table 3 Photophysical parameters used to determine the electron transfer rate constants of all photocatalysts in degassed DMAc. k_{RISC} and $k^{\mathrm{T}}_{\mathrm{nr}}$ were computed using the exact analysis by Adachi and co-workers[57]

	$\varphi_{\mathrm{p},0}$[a]	$\varphi_{\mathrm{d},0}$[b]	$\tau_{\mathrm{p},0}$ (ns)	$\tau_{\mathrm{d},0}$ (ns)	φ_{ISC}	k_{RISC} ($\times10^6$ s^{-1})	$k^{\mathrm{T}}_{\mathrm{nr}}$ ($\times10^6$ s^{-1})	$k^{\mathrm{S}}_{\mathrm{ET}}$ ($\times10^6$ M^{-1} s^{-1})	$k^{\mathrm{T}}_{\mathrm{ET}}$ ($\times10^6$ M^{-1} s^{-1})
PymDMA	0.067	0.0019	13	536	0.57	1.5	1.8	54	80
PymDMDTA	0.035	0.004	8.4	430	0.54	1.5	2.3	49	130
PymDMDMA	0.008	0.001	4.4	579	0.53	0.98	1.7	105	220

[a] Quantum yield of prompt fluorescence at zero quencher. [b] Quantum yield of delayed fluorescence at zero quencher.

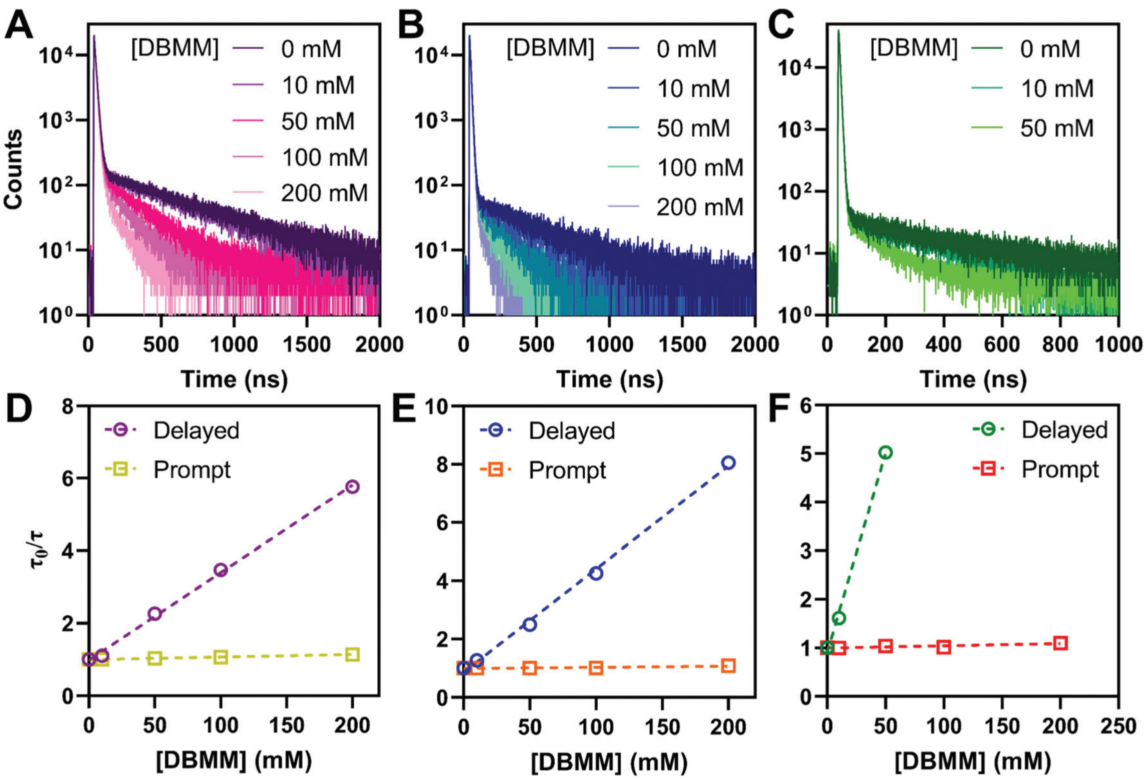

Fig. 4 Transient photoluminescence decay of (A) **PymDMA**, (B) **PymDMDTA**, and (C) **PymDMDMA** dissolved in DMAc (100 μM) with the presence of varying amounts of DBMM initiator. Excited at 380 nm and emission collected at 600 nm. Stern–Volmer plots of the prompt and delayed fluorescence lifetimes as a function of DBMM concentration for (D) **PymDMA**, (E) **PymDMDTA**, and (F) **PymDMDMA**.

states is operative for initiator activation.[58,59] The molar ratio of photocatalyst to initiator used in the experiments ranges between 0.1 and 0.005, comparable to common O-ATRP conditions. Somewhat higher concentrations of photocatalyst than are typical were necessary to account for the low intensity of the emission in DMAc.

The Stern–Volmer eqn (1) is used to extract the rate of singlet electron transfer ($k_{\mathrm{ET}}^{\mathrm{S}}$) from the prompt fluorescence data.

$$\frac{\tau_{\mathrm{p,0}}}{\tau_{\mathrm{p}}} = 1 + k_{\mathrm{ET}}^{\mathrm{S}}\tau_{\mathrm{p,0}}[\mathrm{DBMM}] \tag{1}$$

PymDMDMA has the most rapid singlet electron transfer at 1×10^8 M^{-1} s^{-1} (Table 3). This is still well below the diffusion limit (~10^{10} M^{-1} s^{-1}) indicating that electron transfer is under activation control for this system. Despite the higher driving force for PET in **PymDMDTA**, it has a slightly lower $k_{\mathrm{ET}}^{\mathrm{S}}$ than **PymDMA**. Given the structural similarity of the catalysts, this is surprising, but may reflect a larger reorganization energy for outer-sphere electron transfer in the more sterically encumbered photocatalysts. From DFT, structural reorganization upon the $T_1 \rightarrow D^+$ transition (T_1 and S_1 are assumed to be structurally similar due to their near-degeneracy) is more significant in donor-modified derivatives since the rotation of the pendant aryl groups relative to DMA stabilizes the cation through charge delocalization. For **PymDMDMA**, the average equilibrium dihedral angle between DMA and methoxyphenyl groups decreases from 36.1° in T_1 to 31.6° in D^+. A comparable decrease is observed upon oxidation of **PymDMDTA**.

The rate of electron transfer from the triplet state ($k_{\mathrm{ET}}^{\mathrm{T}}$) is similarly obtained by considering the rate at which the delayed fluorescence is quenched by DBMM. We begin by assuming the majority of excitons are deactivated after a single pass through the triplet state, which is reasonable given that >90% of all excitons are deactivated by fast non-radiative decay even in the absence of DBMM. The intensity ratio of delayed fluorescence to prompt fluorescence has been previously taken as a measure of the average number of cycles through T_1,[60] and is below 1 for all three PCs. The quantum yield of delayed fluorescence (φ_{d}) is then given by the product of the efficiencies of prompt fluorescence (φ_{p}), ISC (φ_{ISC}), and RISC (φ_{RISC}), as an exciton that results in delayed fluorescence will first undergo ISC, then RISC before radiative relaxation from S_1.

$$\varphi_{\mathrm{d}} = \varphi_{\mathrm{p}}\varphi_{\mathrm{ISC}}\varphi_{\mathrm{RISC}} \tag{2}$$

Here, the analysis is simplified by assuming that φ_{p} and φ_{ISC} are not significantly altered by the addition of quencher, which is reasonable given the slow rate of change in the prompt lifetime as a function of [DBMM] (see Fig. S9†). In this case, the ratio $\varphi_{\mathrm{d,0}}/\varphi_{\mathrm{d}}$ can then be written:

$$\frac{\varphi_{\mathrm{d,0}}}{\varphi_{\mathrm{d}}} = \frac{\varphi_{\mathrm{RISC,0}}}{\varphi_{\mathrm{RISC}}}. \tag{3}$$

Because of the low fluorescence quantum yields in these systems, the lifetimes of delayed fluorescence are a more sensitive measure of excited state kinetics than φ_{d}. Assuming the rate constant of delayed fluorescence is unchanged by the DBMM concentration ($k_{\mathrm{d,0}} = k_{\mathrm{d}}$), τ_{d} and φ_{d} are directly proportional over the range of [DBMM] tested ($\varphi_{\mathrm{d}} = k_{\mathrm{d}}\tau_{\mathrm{d}}$),[61–63] which then yields:

$$\frac{\tau_{\mathrm{d,0}}}{\tau_{\mathrm{d}}} = \frac{\varphi_{\mathrm{RISC,0}}}{\varphi_{\mathrm{RISC}}} \tag{4}$$

$\varphi_{\mathrm{RISC,0}}$ is the RISC yield in the absence of DBMM, given by $k_{\mathrm{RISC}}/(k_{\mathrm{RISC}} + k_{\mathrm{nr}}^{\mathrm{T}})$, assuming that phosphorescence from T_1 is negligible. Due to the paltry emission quantum yields in DMAc, non-radiative relaxation of the triplet state cannot be neglected, so the exact analysis of Adachi and co-workers is once again used to calculate the rate constants k_{RISC} and $k_{\mathrm{nr}}^{\mathrm{T}}$ at zero quencher.[57] φ_{RISC} is the RISC yield with DBMM present: $k_{\mathrm{RISC}}/(k_{\mathrm{RISC}} + k_{\mathrm{nr}}^{\mathrm{T}} + k_{\mathrm{ET}}^{\mathrm{T}}[\mathrm{DBMM}])$. Taking their ratio yields a modified version of the Stern–Volmer equation for the delayed fluorescence lifetime:

$$\frac{\tau_{\mathrm{d,0}}}{\tau_{\mathrm{d}}} = 1 + \frac{k_{\mathrm{ET}}^{\mathrm{T}}}{k_{\mathrm{RISC}} + k_{\mathrm{nr}}^{\mathrm{T}}}[\mathrm{DBMM}]. \tag{5}$$

Using this equation, the rates of triplet electron transfer are estimated to be 1.5–3× faster than singlet electron transfer. The trend in triplet electron transfer rates tracks well with the excited state reduction potentials. Coupled with the large ISC yields in DMAc and the low efficiency of back electron transfer in triplet manifolds,[64] these results suggest dominant triplet state activation over the range of initiator concentrations tested.

3.4 O-ATRP performance

The activity of the TADF photocatalysts was evaluated for the polymerization of methyl methacrylate (MMA, $\mathrm{DP_{theo}}$ = 200) and benzyl methacrylate (BnMA, $\mathrm{DP_{theo}}$ = 100). Control experiments were performed without catalyst, or with **PymDMDMA** as catalyst in the absence of initiator, or in the absence of light (Table 4). In the absence of photocatalysts, MMA and BnMA both form high molecular weight, high dispersity ($Đ = M_{\mathrm{w}}/M_{\mathrm{n}}$) polymers (Fig. S10†). The initiator efficiencies ($I^* = M_{\mathrm{n,theo}}/M_{\mathrm{n,exp}}$) are expectedly low. Similar results are obtained in absence of an initiator. In the dark, no polymerization is observed as the catalysts are not sufficiently strong reductants in their ground states to activate DBMM.[65]

The kinetics of polymerization with MMA and BnMA were studied at catalyst loadings of 500 ppm (Fig. 5, see also Fig. S11 and S12†). Hawker has shown that photosensitizers with long-lived excited states for O-ATRP have poor control over polymer dispersity at high catalyst loadings, owing to the persistence of the activator species (^{3}PC*) in solution increasing the concentration of propagating radicals.[14] 500 ppm catalyst loading was chosen to mitigate these effects. In the polymerization of both methacrylic monomers, first-order kinetic behaviour is shown in plots of ln([M$_0$]/[M]) *versus* time for **PymDMDMA** over 8 hours and **PymDMDTA** over 6 hours. For donor-unmodified **PymDMA**, a non-linear plot indicates the rapid onset of termination reactions, likely due to decomposition of its unstable radical cation. The dispersity of

Table 4 Summary of conditions used for and results from the O-ATRP of methyl methacrylate (MMA) and benzyl methacrylate (BnMA). All polymerizations were conducted at temperatures between 28 and 30 °C using 100 μL of monomer in 250 μL total DMAc

Run	PC	Monomer	[M] : [I] : [PC]	Conv.[a] (%)	M_n[b] (kDa)	I^*[c]	Đ[b]
No PC	None	MMA	200 : 1 : 0	12	5090	0.00	2.14
No PC	None	BnMA	100 : 1 : 0	57	308	0.03	2.48
No I	**PymDMDMA**	MMA	200 : 0 : 0.1	13	3450	0.00	2.24
No I	**PymDMDMA**	BnMA	100 : 0 : 0.05	51	1570	0.00	2.67
Dark	**PymDMDMA**	MMA	200 : 1 : 0.1	0	—	—	—
Dark	**PymDMDMA**	BnMA	100 : 1 : 0.05	0	—	—	—
1	**PymDMA**	MMA	200 : 1 : 0.1	66	18.8	0.72	3.11
2	**PymDMDTA**	MMA	200 : 1 : 0.1	75	17.4	0.88	2.06
3	**PymDMDMA**	MMA	200 : 1 : 0.1	89	15.5	1.16	1.75
4	**PymDMDMA**	MMA	100 : 1 : 0.005	67*	6.3*	0.91	1.29
5	**PymDMDMA**	MMA	200 : 1 : 0.01	68*	12.2*	1.14	1.27
6	**PymDMDMA**	MMA	500 : 1 : 0.025	60*	28.2*	0.93	1.51
7	**PymDMDMA**	MMA	1000 : 1 : 0.05	55*	42.2*	0.77	1.70
8	**PymDMDMA**	MMA	200 : 1 : 0.005	72*	13.2*	1.11	1.58
9	**PymDMDMA**	MMA	200 : 1 : 0.002	56*	14.7*	0.78	1.81
10	**Phenox A0202**	MMA	200 : 1 : 0.01	62*	12.4*	1.02	1.51
11	**Phenox A0202**	MMA	200 : 1 : 0.005	65*	14.4*	0.92	1.86
12	**Phenox A0202**	MMA	200 : 1 : 0.002	57*	22.9*	0.51	1.88
13	**PymDMA**	BnMA	100 : 1 : 0.05	81	15.8	0.90	2.04
14	**PymDMDTA**	BnMA	100 : 1 : 0.05	94	15.0	1.09	1.52
15	**PymDMDMA**	BnMA	100 : 1 : 0.05	99	15.3	1.14	1.31

[a] Conversion after 16 (8*) hours irradiation, determined through integration of polymer *versus* monomer signals in the ^{1}H NMR. [b] Determined for the crude polymer after 16 (8*) hours by gel permeation chromatography. [c] $I^* = M_{n,\text{theo}}/M_{n,\text{exp}}$.

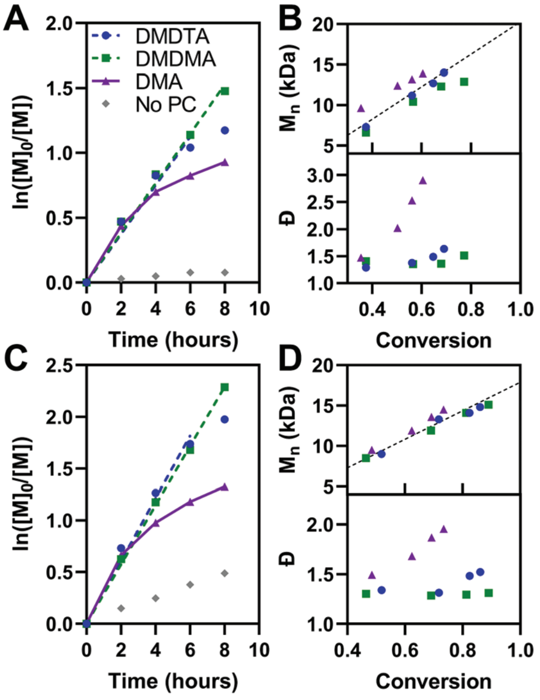

Fig. 5 Polymerization kinetics and plots of molecular weight and dispersity as a function of conversion with different PCs at 500 ppm for (A and B) MMA and (C and D) BnMA. The theoretical molecular weight is given by the dashed black lines in (B) and (D).

the polymer formed with **PymDMA** as the photocatalyst quickly increases at conversions greater than 40%, implying that termination processes outpace initiation.

Donor-modified **PymDMDMA** and **PymDMDTA** polymerize MMA (target molecular weight = 20 kDa) with dispersities below 1.4 up to 75 and 70% conversion, respectively. Further conversion is associated with a steep increase in dispersity (Table 4, entries 2 and 3). Conversely, **PymDMDMA** can polymerize BnMA to 99% conversion with a final dispersity of 1.31 in 16 hours. The syntheses of acrylic polymers of methyl, *n*-butyl, and benzyl acrylate were attempted using **PymDMDMA** and **PymDMDTA**; in all cases poor control over molecular weight was obtained with initiator efficiencies below 0.6 and dispersities above 1.8 after 2 hours (>60% conversion).

The lower control over polymerizations mediated by **PymDMA** compared to its donor-modified derivatives is thought to originate from alkylation of the donor radical cation in the presence of DBMM. When a DMAc solution of **PymDMA** is irradiated with 435 nm light in the presence of 20 equivalents of DBMM, addition of DBMM to the DMA core is observed over 8 hours. In the ^{1}H NMR spectrum (Fig. S11†), the *meta*- and *para*-hydrogen (relative to nitrogen) signals of the DMA donor are transformed from two doublets of doublets into one doublet (with additional hyperfine ^4J coupling), consistent with replacement of either the *meta*- or *para*-hydrogen. By contrast, the ^{1}H NMR spectra of **PymDMDMA** and **PymDMDMTA** are largely unchanged under 435 nm irradiation with DBMM over the same period of time (Fig. S12 and S13†), suggesting it is the *para*-hydrogen that is exchanged in the alkylation of **PymDMA**. Not only does this mode of reactivity lower the initiator efficiency of the polymerization, but it also provides a potential termination mechanism from propagating radicals combining with DMA radical cations, which will cause an increase in the polymer dispersity.

The activity of **PymDMDMA** at low catalyst loadings was evaluated and compared to the phenoxazine-based O-ATRP catalyst **Phenox A0202** reported by Miyake (Fig. S17†).[19] At 50 ppm, **PymDMDMA** performs better in the polymerization of MMA than at 500 ppm loading, with a lower dispersity of 1.27 and good initiator efficiency (Table 4, entry 4). It also has comparatively lower dispersity than **Phenox A0202** at the same loading (Table 4, entry 10). At 50 ppm of **PymDMDMA**, higher target masses of 50 and 100 kDa result in an increase in dispersity compared to the 20 kDa target polymer (Table 4, entries 6 and 7 and Fig. S18†). Decreasing the catalyst loading below 50 ppm is associated with an increase in dispersity for both catalysts, indicating that the deactivator species is not able to achieve a sufficient concentration. At 10 ppm, both catalysts produce PMMA with dispersities over 1.8 and initiator efficiencies below 0.78 after 8 hours (entries 9 and 12).

To evaluate the chain-end retention provided by O-ATRP with **PymDMDMA**, a PMMA-*b*-p(BnMA) block copolymer was synthesized. 10 kDa PMMA was first prepared using 100 ppm **PymDMDMA** and halting the polymerization at 50% conversion to give macroinitiator with dispersity 1.18 after precipitation in ethanol. Chain extension with p(BnMA) was then attempted with 500 ppm **PymDMDMA**. After 8 hours, the conversion of BnMA was 93% by ^{1}H NMR, similar to the polymerization using DBMM initiator. The ^{1}H NMR spectrum of the precipitated polymer contains distinct resonances at δ 7.30 and 4.90 ppm of p(BnMA) and 3.62 ppm for the methyl ester of PMMA. In the DOSY spectrum of the block copolymer, all three resonances diffuse at the same level, with a narrow dispersion of diffusion coefficients between 3.6 and 3.9 × 10^{-10} m^2 s^{-1} (Fig. 6A), suggesting covalent linkage of PMMA and p(BnMA) blocks. Integration of the ^{1}H NMR spectrum (Fig. S19†) yields an excess of BnMA compared to theory (DP 119 compared to 93), suggesting that as much as 22% of macroinitiator chains are not re-initiated. While a clear separation between macroinitiator and block copolymer traces is observed by GPC (Fig. 6B), significant shouldering at low molecular weight is responsible for an increase in dispersity upon block formation. This is likely due to the presence of dead macroinitiator chains, as O-ATRP is not a truly living process and some degree of termination is to be expected.

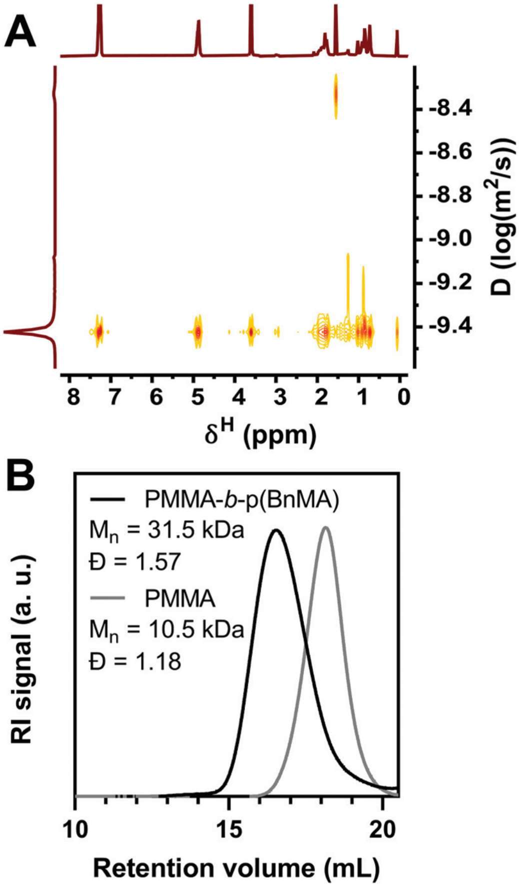

Fig. 6 (A) DOSY spectrum of PMMA-*b*-p(BnMA) in $CDCl_3$. (B) RI Chromatogram of PMMA macroinitiator and PMMA-*b*-p(BnMA).

4. Conclusions

The promise of TADF for metal-free photocatalytic transformations relies on a strong understanding of structure–activity relationships. In this study, modification of the donor group used in TADF was investigated with respect to the ability to participate in dissociative and associative electron transfer for visible-light promoted O-ATRP. While the stability of the radical cation is found to be the strongest determining factor for controlled polymerization, significant differences amongst donor-modified catalysts are related to variation in the rates of photoinduced electron transfer. Our results are consistent with previous studies that posit both singlet and triplet electron transfer as initiation mechanisms, with the reduced singlet–triplet energy gap in TADF emitters benefitting both the yield and driving force of triplet electron transfer. The ability to predict these driving forces based on theoretical modelling is promising, as computations can inform the types of donors, acceptors, and their modifications to design the most efficient catalysts.

The results of this study should be applicable to any of the donors commonly used in TADF. Carbazole, a widely used donor, is known to have irreversible oxidative chemistry which may hinder its applications in photoreductive catalysis.[66] Donors with reversible oxidations, such as phenothiazine, phenoxazine, and phenazine, are still susceptible to turnover-limiting photosubstitution chemistry in the absence of appropriate donor-modification strategies. We anticipate that the widespread adoption of TADF photocatalysts in organic synthesis will greatly benefit from the development of more robust donor and acceptor fragments with increased potential for high conversions, reduced side-reactivity and catalyst recyclability.

Author contributions

All authors have given approval to the final version of the manuscript.

Conflicts of interest

There are no conflicts to declare.

Acknowledgements

We wish to thank Dr Maria Ezhova for performing the DOSY NMR study. The authors thank the Natural Sciences and Engineering Council of Canada (NSERC) for financial support. A. M. P. and S. H. H. thank NSERC for a Canada Graduate Scholarship and Undergraduate Student Research Award, respectively. Z. M. H. gratefully acknowledges support from the Canada Research Chairs Program.

Notes and references

1 J. Nicolas, Y. Guillaneuf, C. Lefay, D. Bertin, D. Gigmes and B. Charleux, *Prog. Polym. Sci.*, 2013, **38**, 63–235.

2 J. Chiefari, Y. K. Chong, F. Ercole, J. Krstina, J. Jeffery, T. P. T. Le, R. T. A. Mayadunne, G. F. Meijs, C. L. Moad, G. Moad, E. Rizzardo and S. H. Thang, *Macromolecules*, 1998, **31**, 5559–5562.

3 K. Matyjaszewski, *Macromolecules*, 2012, **45**, 4015–4039.

4 W. A. Braunecker and K. Matyjaszewski, *Prog. Polym. Sci.*, 2007, **32**, 93–146.

5 J. S. Wang and K. Matyjaszewski, *J. Am. Chem. Soc.*, 1995, **117**, 5614–5615.

6 K. Matyjaszewski, *Adv. Mater.*, 2018, **30**, 1706441.

7 W. Jakubowski and K. Matyjaszewski, *Angew. Chem., Int. Ed.*, 2006, **45**, 4482–4486.

8 A. Anastasaki, V. Nikolaou, G. Nurumbetov, P. Wilson, K. Kempe, J. F. Quinn, T. P. Davis, M. R. Whittaker and D. M. Haddleton, *Chem. Rev.*, 2016, **116**, 835–877.

9 K. Matyjaszewski, W. Jakubowski, K. Min, W. Tang, J. Huang, W. A. Braunecker and N. V. Tsarevsky, *Proc. Natl. Acad. Sci. U. S. A.*, 2006, **103**, 15309–15314.

10 M. A. Tasdelen, M. Uygun and Y. Yagci, *Macromol. Chem. Phys.*, 2010, **211**, 2271–2275.

11 M. A. Tasdelen, M. Ciftci and Y. Yagci, *Macromol. Chem. Phys.*, 2012, **213**, 1391–1396.

12 Q. Yang, F. Dumur, F. Morlet-Savary, J. Poly and J. Lalevée, *Macromolecules*, 2015, **48**, 1972–1980.

13 S. Dadashi-Silab, K. Kim, F. Lorandi, G. Szczepaniak, S. Kramer, L. Peteanu and K. Matyjaszewski, *ACS Macro Lett.*, 2022, **11**, 376–381.

14 B. P. Fors and C. J. Hawker, *Angew. Chem., Int. Ed.*, 2012, **51**, 8850–8853.

15 N. J. Treat, H. Sprafke, J. W. Kramer, P. G. Clark, B. E. Barton, J. Read de Alaniz, B. P. Fors and C. J. Hawker, *J. Am. Chem. Soc.*, 2014, **136**, 16096–16101.

16 Q. Ma, J. Song, X. Zhang, Y. Jiang, L. Ji and S. Liao, *Nat. Commun.*, 2021, **12**, 429.

17 J. C. Theriot, C. H. Lim, H. Yang, M. D. Ryan, C. B. Musgrave and G. M. Miyake, *Science*, 2016, **352**, 1082–1086.

18 B. L. Buss, C. Lim and G. M. Miyake, *Angew. Chem., Int. Ed.*, 2020, **59**, 3209–3217.

19 B. G. McCarthy, R. M. Pearson, C. H. Lim, S. M. Sartor, N. H. Damrauer and G. M. Miyake, *J. Am. Chem. Soc.*, 2018, **140**, 5088–5101.

20 A. Allushi, S. Jockusch, G. Yilmaz and Y. Yagci, *Macromolecules*, 2016, **49**, 7785–7792.

21 X. Liu, L. Zhang, Z. Cheng and X. Zhu, *Polym. Chem.*, 2016, **7**, 689–700.

22 C. Wu, N. Corrigan, C.-H. Lim, W. Liu, G. M. Miyake and C. Boyer, *Chem. Rev.*, 2022, **122**, 5476–5518.

23 P. Lu, V. K. Kensy, R. L. Tritt, D. T. Seidenkranz and A. J. Boydston, *Acc. Chem. Res.*, 2020, **53**, 2325–2335.

24 C. Wu, K. Jung, Y. Ma, W. Liu and C. Boyer, *Nat. Commun.*, 2021, **12**, 478.

25 N. Corrigan, S. Shanmugam, J. Xu and C. Boyer, *Chem. Soc. Rev.*, 2016, **45**, 6165–6212.

26 E. E. Stache, V. Kottisch and B. P. Fors, *J. Am. Chem. Soc.*, 2020, **142**, 4581–4585.

27 Z. Huang, Y. Gu, X. Liu, L. Zhang, Z. Cheng and X. Zhu, *Macromol. Rapid Commun.*, 2017, **38**, 1600461a.

28 H. Uoyama, K. Goushi, K. Shizu, H. Nomura and C. Adachi, *Nature*, 2012, **492**, 234–238.

29 M. A. Bryden and E. Zysman-Colman, *Chem. Soc. Rev.*, 2021, **50**, 7587–7680.

30 F. Fang, L. Zhu, M. Li, Y. Song, M. Sun, D. Zhao and J. Zhang, *Adv. Sci.*, 2021, 2102970.

31 N. R. Paisley, C. M. Tonge and Z. M. Hudson, *Front. Chem.*, 2020, **8**, 229.

32 F. Ni, N. Li, L. Zhan and C. Yang, *Adv. Opt. Mater.*, 2020, **8**, 1902187.

33 A. M. Polgar and Z. M. Hudson, *Chem. Commun.*, 2021, **57**, 10675–10688.

34 V. K. Singh, C. Yu, S. Badgujar, Y. Kim, Y. Kwon, D. Kim, J. Lee, T. Akhter, G. Thangavel, L. S. Park, J. Lee, P. C. Nandajan, R. Wannemacher, B. Milián-Medina, L. Lüer, K. S. Kim, J. Gierschner and M. S. Kwon, *Nat. Catal.*, 2018, **1**, 794–804.

35 X. Pan, C. Fang, M. Fantin, N. Malhotra, W. Y. So, L. A. Peteanu, A. A. Isse, A. Gennaro, P. Liu and K. Matyjaszewski, *J. Am. Chem. Soc.*, 2016, **138**, 2411–2425.

36 J. J. Devery, J. J. Douglas, J. D. Nguyen, K. P. Cole, R. A. Flowers and C. R. J. Stephenson, *Chem. Sci.*, 2015, **6**, 537–541.

37 B. McCarthy, S. Sartor, J. Cole, N. Damrauer and G. M. Miyake, *Macromolecules*, 2020, **53**, 9208–9219.

38 Z. Zhang, W. Chen, Y. Zhang, Y. Wang, Y. Tian, L. Fang and X. Ba, *Macromolecules*, 2021, **54**, 4633–4640.

39 D. A. Corbin, K. O. Puffer, K. A. Chism, J. P. Cole, J. C. Theriot, B. G. McCarthy, B. L. Buss, C. H. Lim, S. R. Lincoln, B. S. Newell and G. M. Miyake, *Macromolecules*, 2021, **54**, 4507–4516.

40 S. Grotjahn and B. König, *Org. Lett.*, 2021, **23**, 3146–3150.

41 D. Kong, M. Munch, Q. Qiqige, C. J. C. Cooze, B. H. Rotstein and R. J. Lundgren, *J. Am. Chem. Soc.*, 2021, **143**, 2200–2206.

42 N. Lin, J. Qiao, L. Duan, L. Wang and Y. Qiu, *J. Phys. Chem. C*, 2014, **118**, 7569–7578.

43 C. M. Cardona, W. Li, A. E. Kaifer, D. Stockdale and G. C. Bazan, *Adv. Mater.*, 2011, **23**, 2367–2371.

44 C. Lee, W. Yang and R. G. Parr, *Phys. Rev. B: Condens. Matter Mater. Phys.*, 1988, **37**, 785–789.

45 A. D. Becke, *J. Chem. Phys.*, 1993, **98**, 5648–5652.

46 P. Winget, C. J. Cramer and D. G. Truhlar, *Theor. Chem. Acc.*, 2004, **112**, 217–227.

47 J.-D. Chai and M. Head-Gordon, *Phys. Chem. Chem. Phys.*, 2008, **10**, 6615.

48 S. Hirata and M. Head-Gordon, *Chem. Phys. Lett.*, 1999, **314**, 291–299.

49 M. J. G. Peach, M. J. Williamson and D. J. Tozer, *J. Chem. Theory Comput.*, 2011, **7**, 3578–3585.

50 N. T. Maitra, *J. Chem. Phys.*, 2005, **122**, 234104.

51 P. Mori-Sánchez, A. J. Cohen and W. Yang, *Phys. Rev. Lett.*, 2008, **100**, 146401.

52 H. Sun, C. Zhong and J.-L. Brédas, *J. Chem. Theory Comput.*, 2015, **11**, 3851–3858.

53 S. Hirata, Y. Sakai, K. Masui, H. Tanaka, S. Y. Lee, H. Nomura, N. Nakamura, M. Yasumatsu, H. Nakanotani, Q. Zhang, K. Shizu, H. Miyazaki and C. Adachi, *Nat. Mater.*, 2015, **14**, 330–336.

54 H. Kaji, H. Suzuki, T. Fukushima, K. Shizu, K. Suzuki, S. Kubo, T. Komino, H. Oiwa, F. Suzuki, A. Wakamiya, Y. Murata and C. Adachi, *Nat. Commun.*, 2015, **6**, 8476.

55 R. Komatsu, H. Sasabe, Y. Seino, K. Nakao and J. Kido, *J. Mater. Chem. C*, 2016, **4**, 2274–2278.

56 R. Komatsu, H. Sasabe, K. Nakao, Y. Hayasaka, T. Ohsawa and J. Kido, *Adv. Opt. Mater.*, 2017, **5**, 1600675.

57 Y. Tsuchiya, S. Diesing, F. Bencheikh, Y. Wada, P. L. dos Santos, H. Kaji, E. Zysman-Colman, I. D. W. Samuel and C. Adachi, *J. Phys. Chem. A*, 2021, **125**, 8074–8089.

58 D. Koyama, H. J. A. Dale and A. J. Orr-Ewing, *J. Am. Chem. Soc.*, 2018, **140**, 1285–1293.

59 A. Bhattacherjee, M. Sneha, L. Lewis-Borrell, G. Amoruso, T. A. A. Oliver, J. Tyler, I. P. Clark and A. J. Orr-Ewing, *J. Am. Chem. Soc.*, 2021, **143**, 3613–3627.

60 C. Baleizão and M. N. Berberan-Santos, *J. Chem. Phys.*, 2007, **126**, 204510.

61 K. Goushi, K. Yoshida, K. Sato and C. Adachi, *Nat. Photonics*, 2012, **6**, 253–258.

62 F. B. Dias, *Philos. Trans. R. Soc., A*, 2015, **373**, 20140447.

63 Y. Tao, K. Yuan, T. Chen, P. Xu, H. Li, R. Chen, C. Zheng, L. Zhang and W. Huang, *Adv. Mater.*, 2014, **26**, 7931–7958.

64 N. A. Romero and D. A. Nicewicz, *Chem. Rev.*, 2016, **116**, 10075–10166.

65 N. D. Dolinski, Z. A. Page, E. H. Discekici, D. Meis, I. H. Lee, G. R. Jones, R. Whitfield, X. Pan, B. G. McCarthy, S. Shanmugam, V. Kottisch, B. P. Fors, C. Boyer, G. M. Miyake, K. Matyjaszewski, D. M. Haddleton, J. R. de Alaniz, A. Anastasaki and C. J. Hawker, *J. Polym. Sci., Part A: Polym. Chem.*, 2019, **57**, 268–273.

66 K. Karon and M. Lapkowski, *J. Solid State Electrochem.*, 2015, **19**, 2601–2610.